Urban Climate 48 (2023) 101389

Contents lists available at ScienceDirect

Urban Climate

journal homepage: www.elsevier.com/locate/uclim

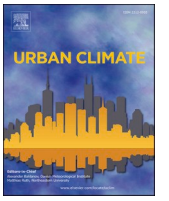

Mega-city development impact on hourly extreme rainfall over the South China Greater Bay Area under near-future climate warming

Chenxi Hu [a], Chi-Yung Tam [a,f,*], Xinwei Li [b,h], Kangning Huang [c], Chao Ren [b], Kwun Yip Fung [a,g], Ziqian Wang [d,e]

[a] Earth System Science Programme, the Chinese University of Hong Kong, Hong Kong, China
[b] Faculty of Architecture, the University of Hong Kong, Hong Kong, China
[c] New York University Shanghai, Shanghai, China
[d] School of Atmospheric Sciences, and Guangdong Province Key Laboratory for Climate Change and Natural Disaster Studies, Sun Yat-sen University, Zhuhai, China
[e] Southern Marine Science and Engineering Guangdong Laboratory (Zhuhai), Zhuhai, China
[f] Shenzhen Research Institute, the Chinese University of Hong Kong, Shenzhen, China
[g] Geological Sciences, Jackson School of Geoscience, The University of Texas at Austin, Austin, TX, USA
[h] Planning Department, the Government of HKSAR, Hong Kong, China

ARTICLE INFO

Keywords:
Urbanization
Extreme precipitation
Climate change
Urban Heat Island effect

ABSTRACT

The impacts of near-future urban development and global warming forcing on hourly extreme rainfall over the South China Greater Bay Area (GBA) area have been investigated, by dynamically downscaling General Circulation Model (GCM) outputs using the Weather Research and Forecasting Model (WRF) at convection-permitting resolution, coupled with an Urban Canopy Model (UCM). Three downscaling experiments corresponding to different urban land cover (1999 and projected 2030) and climate (1951-to-2000 and 2001-to-2050 GCM simulations) were designed. Effects of near-future climate change and 1999-to-2030 urban development on GBA extreme precipitation were then examined, using boundary conditions derived from GBA extreme rainfall events in the Geophysical Fluid Dynamics Laboratory Earth System Model (GFDL-ESM2M) historical and RCP8.5 simulations. Results show that climate change and rapid urban development forcing have comparable positive effects on the intensity as well as heavy hourly rainfall probability over the GBA urban area. Global warming tends to increase heavy rainfall probability (from 40 to 60 mm/h) by about 1.3 to 1.8 times, but at the same time suppress the probability of light rainfall (from 1 to 10 mm/h) by about 20%. Urban development increases urban rainfall probability within the whole range of intensity, with frequency for very heavy rainfall (> 90 mm/h) almost doubled. It is worth mentioning that impacts due to rapid urban development can be as important as global warming forcing in the near future in exacerbating hourly extreme rainfall over the GBA coastal megacity.

1. Introduction

There is now ample evidence that anthropogenic activities can exacerbate meteorological hazards such as heat waves and extreme

* Corresponding author at: Earth System Science Programme, the Chinese University of Hong Kong, Hong Kong, China.
E-mail address: francis.tam@cuhk.edu.hk (C.-Y. Tam).

https://doi.org/10.1016/j.uclim.2022.101389
Received 10 April 2022; Received in revised form 7 December 2022; Accepted 14 December 2022
Available online 12 January 2023

rainfall. Since the last century, many places have experienced rapid urbanization (Hannah, 2018), which modulates local climate of cities, leading to changes in surface high temperature (Mohajerani et al., 2017; Luo and Lau, 2017), precipitation (Huff and Changnon, 1972; Han et al., 2014), and circulation (Li et al., 2016; Fan et al., 2018). It is well known that more shortwave radiation is absorbed over the city area as a result of modified land use, lower surface albedo, and urban morphology (Soltani and Sharifi, 2017). Anthropogenic heat (AH) released from buildings, traffic, and human populations can also promote the formation of urban heat island (UHI) (Shahmohamadi et al., 2011), resulting in higher temperature (Mohajerani et al., 2017) and environment conductive to convection (Baik et al., 2001; Han and Baik, 2008). Many studies show that urbanization can enhance rainfall intensity downstream of some cities (Changnon, 1968; Shepherd and Burian, 2003; Lin et al., 2008; Shem and Shepherd, 2009). However, this result might depend on the UHI intensity; recent studies for Beijing demonstrate that strong UHI can increase rainfall directly over the downtown area, while on weak UHI days, precipitation tends to be bifurcated and avoids the city center (Dou et al., 2015; Zhang et al., 2017). AH released over megacities also plays a role in intensifying extreme rainfall and local convection (Holst et al., 2016; Holst et al., 2017; Fung et al., 2021; Hu et al., 2021). On the other hand, impervious surface within a city means less water permeability and surface evaporation, which results in lower surface moisture and decreased latent heat flux to the atmosphere (Bornstein, 1968; Oke, 1988). Previous studies pointed out that decreased water content can reduce convective available potential energy (CAPE), and hence the total precipitation amount over the Beijing urban area (Guo et al., 2006; Zhang et al., 2009a). For coastal urban locales, enhanced surface temperature induced by urbanization can lead to stronger low-level flow from the ocean, which transports water vapor to the urban area. This contributes to stronger extreme precipitation intensity in some coastal cities such as Tokyo, Osaka, and the South China Greater Bay Area (GBA) megacity (Fung et al., 2021; Hu et al., 2021; Kusaka et al., 2014; Shimadera et al., 2015; Wang et al., 2015; Xiao et al., 2020; Wen et al., 2020).

At the same time, global temperature is rising rapidly due to climate change caused by anthropogenic greenhouse gas emissions (Knutson et al., 2017), with some climate projections giving even stronger warming trends in the future (Meehl et al., 2007). Under a warmer climate, the enhanced thermal stability is likely to suppress light precipitation over the monsoon area and contiguous US (Chou et al., 2012; Hsu et al., 2012; Dai et al., 2017) or even total precipitation in some subtropical areas such as Japan (Chou and Neelin, 2004; Kenshi et al., 2018). On the other hand, according to the Clausius-Clapeyron (CC) relationship, the saturated vapor pressure increases by about 7% per degree of near-surface warming, which indicates the atmosphere can accommodate more water vapor in a warmer climate. Future heavy rainfall will become stronger and more frequent as the atmosphere becomes more humid (Hsu et al., 2012; Marta and Jan, 2020; Tabari, 2020). Indeed, many places have previously noted rising trends in extreme rainfall (Iwashima and Yamamoto, 1993; Karl and Knight, 1998; Myhre et al., 2019). Numerical simulations focus on the relationship between global warming and extreme rainfall also produce results consistent with observations, with changes in the intensity of extreme rainfall generally exceeding those in the annual mean in the tropical areas (Fung et al., 2021; Chen, 2013; Kharin et al., 2007).

Since the early 1980s, the GBA region, which known as a megacity cluster located in southern China, has witnessed tremendous urbanization. During the summer monsoon season, there is heavy precipitation, mainly brought on by severe thunderstorm systems and tropical cyclones (TC) (Wai et al., 1995; Chang et al., 2012). Observations show that both the intensity and frequency of GBA extreme rainfall have increased (>5% per decade) over most GBA mega-cities from 1971 to 2016 (Yan et al., 2020), concurrent with regional urban expansion (Wang et al., 2015). There are in fact robust increases of hourly extreme rainfall by strong UHI in the urban GBA due to various synoptic systems (Wu et al., 2019; Sun et al., 2021). An increasing trend of both the strength and frequency of extreme rainfall has been observed over South China, while the number of rainy days has decreased at the same time (Meehl et al., 2007; Zhang et al., 2009b; Wong et al., 2011). Results from numerical modeling also demonstrate that global warming can significantly increase both the intensity and frequency of extreme rainfall over GBA (Fung et al., 2021).

In this work, we investigate: (1) how urban development and global warming together might affect the characteristics of intense precipitation over GBA in the coming decades, and (2) whether the effects of urban development and climate change on GBA urban extreme rainfall are comparable. A recent study utilized a high-resolution model, with various types of urban land use incorporated, for assessing the impacts of both urban development and global warming on thermal comfort within GBA (Wang et al., 2021). To our knowledge, this is the first study using a similar approach to examine their twin impacts on GBA extreme rainfall. In particular, a convection-permitting regional model with simulated urban canopy over city regions was used to perform dynamical downscaling of General Circulation Model (GCM) outputs from historical runs and near-future climate projections. Moreover, a 2030 land use dataset over the GBA region is considered, which is derived from a land use prediction model that adopts "training" based on historical GBA land use (Huang et al., 2021). This helps quantifying the magnitudes of extreme rainfall changes induced by anthropogenic activities (urban development and climate change) in the near future over GBA mega-city. Results based on similar modeling strategies can serve as a scientific basis for local policy makers to develop climate change adaptation plans in relation to the hydroclimate projections.

2. Methodology

2.1. Data description and model evaluation

The Weather Research and Forecasting (WRF) model version 3.8.1 with the Advanced Research WRF dynamic core (Skamarock et al., 2008) coupled with the single-layer urban canopy model (SLUCM) (Kusaka and Kimura, 2004), was used to dynamical downscale extreme precipitation events over the GBA area, as identified from the Geophysical Fluid Dynamical Laboratory Earth System model version 2 (GFDL-ESM2M (Dunne et al., 2012; Dunne et al., 2013)) historical run (1950–2005) and the RCP8.5 projection (2006–2050). The GFDL-ESM2M atmospheric component has a horizontal resolution of 2^{o} x 2.5^{o} in latitudes and longitudes, respectively, 24 vertical levels, and its ocean component is the Modular Ocean Model version 4 (MOM4). The model gives reasonable

performances in simulating the East Asia monsoon circulation (McSweeney et al., 2015).

To assess the model performance, precipitation in GFDL-ESM2M is assessed by comparing model summertime mean rainfall from 1951 to 2007 with the station-based APHRODITE (Asian Precipitation Highly Resolved Observational Data Integration Toward Evaluation) land precipitation data (Yotagai et al., 2012), as well as model summertime mean rainfall from 1998 to 2013 by comparison with the Tropical Rainfall Measuring Mission (TRMM)-3B42 multi-satellite precipitation products (Huffman et al., 2014). Fig. 1 depicts the climatological warm-season (May, June, July, August, September) daily precipitation from (a) GFDL-ESM2M and (b) APHRODITE from 1951 to 2007, (c) GFDL-ESM2M and (d) TRMM from 1998 to 2013, with the red box representing the South China region. Major features in East Asia, such as heavy rainfall in the south Tibet Plateau, the Meiyu-Baiu rainband, and Southeast Asia, are well reproduced by the model, and the GCM rainfall in South China lies within the reasonable range based on TRMM and APHRODITE, which are 2 independent rainfall products.

Moreover, to summarize the model's performances in different circulation variables, Fung et al. (Fung et al., 2018) compared model products including temperature (Ta), geopotential height (H), U-wind (Ua), and V-wind (Va) with their counterparts from the ERA-Interim reanalysis data (Dee et al., 2011). Fig. S1 compares the monthly mean values of temperature, geopotential height, U-wind, and V-wind variables from GFDL-ESM2M to those from ERA-interim, for May, June, July, August, and September from 1979 to 2014 over the East Asia region (15^{o} to 50^{o}N, 90^{o} to 140°E). It is found that GFDL-ESM2M systematically underestimates the near-surface (mid-tropospheric) temperature by about 1 to 3 K. In particular, there is moderate cold bias in the low levels, but the bias becomes stronger at 500 hPa. Such a cold bias also results in an underestimation of geopotential height in the mid to upper troposphere. On the other hand, U-wind and V-wind are simulated well throughout the troposphere. Fig. S2 depicts the climatological warm-season (May–September) mean distribution of 500 hPa temperature, 500 hPa geopotential height, and 850 hPa temperature with u,v wind circulation. It is noteworthy that GFDL-ESM2M performs reasonably well in the warm-season low-level wind circulation in Asia (e.g., Indian Ocean and Central China). Features such as the western Pacific subtropical high and the monsoon circulation from equator to the South China Sea are also captured, as reflected by the 850 hPa wind field. However, due to its tropical easterlies being too strong over the western Pacific, the model tends to give low-level easterlies rather than westerlies in the South China Sea. Overall, the GFDL-ESM2M outputs give reasonable performance in atmospheric parameters over East Asia. More detailed model evaluation can be found in Fung (Fung et al., 2018).

2.2. *WRF setting and extreme case selection*

Physical parameterizations in WRF include the use of the NOAH Land Surface Model (LSM) (for supporting SLUCM in the model environment (Chen and Dudhia, 2001; Tewari et al., 2008)), the Rapid Radiative Transfer Model for General Circulation Model (RRTMG) for longwave radiation (Iacono et al., 2008), the short wave radiation scheme by Dudhia (Dudhia, 1989), the WRF single-

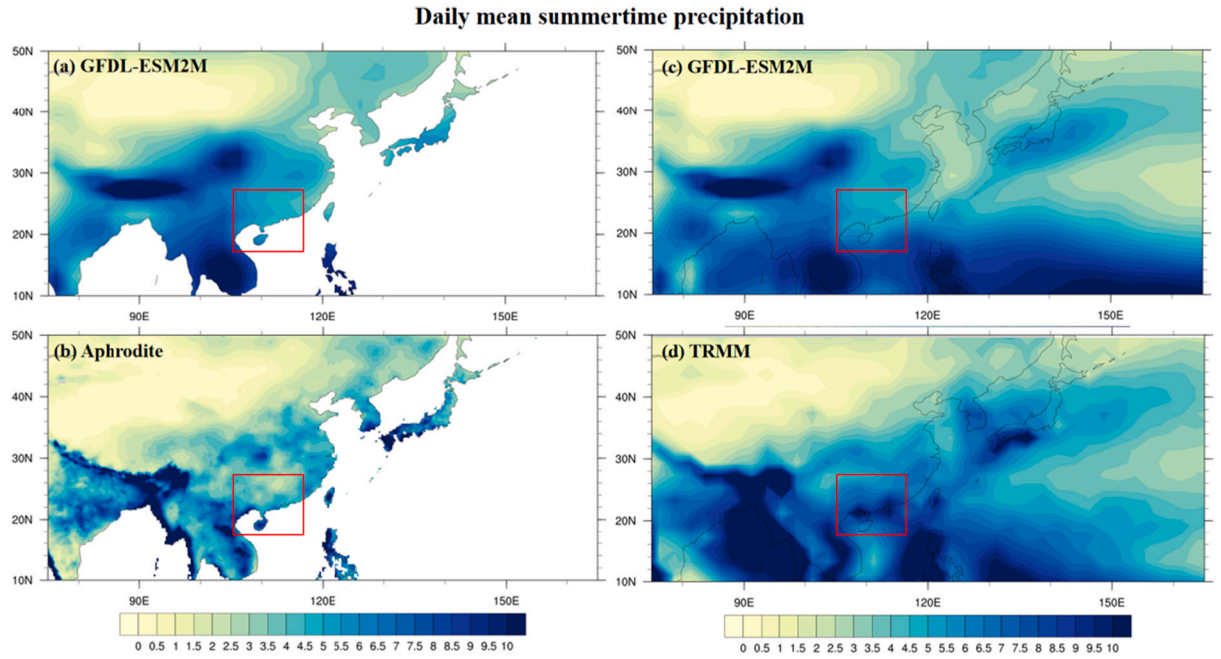

Fig. 1. Climatological daily mean precipitation intensity (MJJAS) from 1951 to 2007 based on (a) GFDL-ESM2M historical and (b) APHRODITE data; Climatological daily mean precipitation intensity (MJJAS) from 1998 to 2013 based on (c) GFDL-ESM2M historical and (d) TRMM data. The red box marked the South China region (17^{o}-27^{o}N,105^{o}-117°E). (For interpretation of the references to colour in this figure legend, the reader is referred to the web version of this article.)

moment 6-class microphysics scheme (Hong and Lim, 2006), Eta similarity theory for surface layer options (Janjic, 2002), the Bougeault-Lacarrere planetary boundary layer scheme (Bougeault and Lacarrere, 1989), and the simplified Arakawa-Schubert (SAS) GFS cumulus parameterization (Han and Pan, 2011) (for the outermost domain only). Fig. 2a shows the nested domains for the downscaling experiments, which cover East Asia/western north Pacific (2.23–43.82°N, 70.81–147.05°E, at 50 km × 50 km resolution), South China (19.94–27.09°N, 110.68–117.60°E, at 10 km × 10 km resolution) and GBA (21.5–23.83°N, 112.51–115.04°E, at 2 km × 2 km resolution). There are 39 vertical levels, reaching ~10 hPa.

Extreme rainfall events were taken from the historical as well as RCP8.5 simulations of GFDL-ESM2M. Daily mean precipitation averaged over the land area of South China region (17-27°N, 105-117°E) was first computed for historical and near-future runs separately. Days during which daily rainfall > the 99th percentile (based on rainfall on wet days, when rain rate > 0.1 mm/day) were defined as extreme rain days. Note that most of the extreme rainfall cases occur during the summer (MJJAS) in the GFDL-ESM2M historical as well as RCP8.5 simulations, consistent with TRMM (Fung et al., 2021). Second, extreme events were identified such that they cover extreme rain days (top 1%) plus 2 days before and after the extreme days (see below). Third, extreme cases in relation to tropical cyclones (TC) were removed. Finally, 60 extreme cases in the warm season of May to September, not related to TC-like systems (hereinafter referred to as non-TC cases) were selected. 30 extreme cases were selected from the historical era (1951–2000), and 30 extreme cases from the near-future era (2001–2050). GCM outputs from these cases were then downscaled by WRF, with integrations starting from 48 h prior to the extreme rain day to 48 h after the extreme rain day.

2.3. Local climate zone (LCZ) data, UCM and model experiments

Altogether, three sets of experiments using WRF-SLUCM were conducted: in 99LS-HIS, extreme events from the GFDL-ESM2M

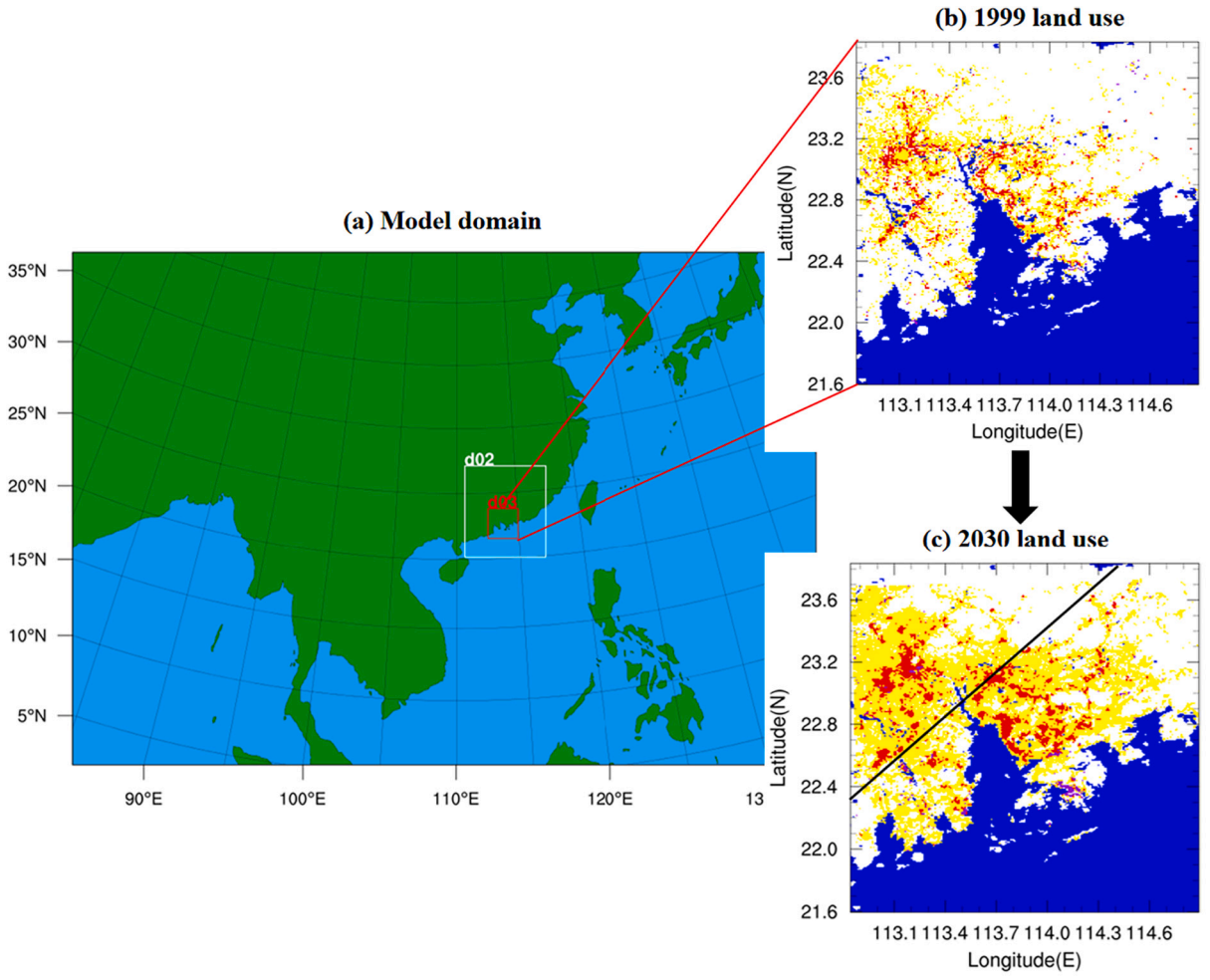

Fig. 2. (a) Nested domains for the WRF simulations. (b) Land use categories of 1999 in the innermost domain with "Low Intensity Residence", "High Intensity Residence", and "Commercial and Industrial" locations indicated by yellow, red, and purple shading. Same as (b) but for projected 2030 urban land use. Black line indicates the cross-sectional plane for Fig. 9. (For interpretation of the references to colour in this figure legend, the reader is referred to the web version of this article.)

historical climate run (1951–2000) were dynamical downscaled, with prescribed 1999 urban land use; in 99LS-FUT, extreme rainfall cases from the near-future (2001–2050) run with 1999 urban land were simulated; finally, in 30LS-FUT, the same sets of extreme rain cases as in 99LS-FUT were downscaled, with 2030 urban land use information in SLUCM. For the highly urbanized GBA region, detailed land use/land cover change (LULCC) types in 1999 and the near-future projection in 2030 built on the WUDAPT protocol were developed (Ching et al., 2018; Wang et al., 2019) with a spatial resolution of 1 km × 1 km, and classified according to the local climate zone (LCZ) scheme (Stewart and Oke, 2012). LCZ classification includes ten types for urban land use (namely Compact High-Rise, Compact Mid-Rise, Compact Low-Rise, Open High-Rise, Open Mid-Rise, Open Low-Rise, Lightweight Low-Rise, Large Low-Rise, Sparsely Built, Heavy Industry), and seven types for natural land use (Dense Trees, Scattered Trees, Bush and Scrub, Low Plants, Bare Rock or Paved, Bare Soil or Sand, and Water). Each LCZ type has its own set of UCM parameters and attributes (Stewart and Oke, 2014) (such as surface albedo, building height, sky view factor, etc.), which are specified based on data from the GBA megacity area. Urban land use information of GBA in 1999 (the historical era) and in 2030 (the projected near-future era) were prescribed differently in the model (Wang et al., 2019).

For the urban land use in 2030, the near future LCZ maps over the GBA region are projected by Huang (Huang et al., 2021), with a land-use land cover change (LULCC) model: the Geographical Simulation and Optimization System (GeoSOS) – Future Land Use Simulation (FLUS) model (Liu et al., 2017; Chen et al., 2014) being used based on the historical LCZ maps and the interaction between different land uses. First, a data mining technique, namely the Artificial Neural Network (ANN), is used to learn the occurrence probability for each land use from historical LCZ maps, using geographical factors derived from the current LCZ maps such as slopes, aspect, elevation, distance to city centers, distance to roads, and distance to highways. Then, future demands for urban land-use and land-cover changes are predicted based on trajectories of demographic and socioeconomic developments. Finally, a Cellular Automata (CA) model is used to simulate the land-use conversions based on current LCZ maps (2014 LCZ maps), with the occurrence and neighborhood influence probability being repeated until future demands are met. The projected near-future maps are then generated by the CA model.

To simplify the prediction scheme and decrease the prediction uncertainties, ten types of urban LCZ were regrouped into three types: “Low Intensity Residence” (type 1), “High Intensity Residence” (type 2), and “Commercial and Industrial” (type 3). Type 1 comprises Open Mid Rise, Open Low Rise, Sparsely Built, Open High Rise, Lightweight Low Rise, and Large Low Rise. Type 2 consists of Compact Mid Rise and Compact Low Rise. Type 3 includes Compact High Rise and Heavy Industry. This land use regrouping method is based on the AH value for each urban LCZ: e.g., Compact High Rise and Heavy Industry with the highest AH (> 150 W/m^2) are regrouped as “Commercial and Industrial”; similarly, Urban LCZs with AH <25 W/m^2 are regrouped as “Low Intensity Residence”. Table 1 gives the UCM parameters prescribed for these three land use types, with values recomputed based on those provided by WUDAPT for GBA. Fig. 2 are the 1999 and 2030 urban land use distributions (after re-grouping) in the innermost model domain, with yellow, red, and purple indicating type 1, 2, and 3 urban land use, respectively.

3. Results

3.1. GFDL-ESM2M climatology statistics

The projected changes of warm-season (MJJAS) climate characteristics from GFDL-ESM2M historical and RCP8.5 simulation are first examined. Fig. 3a shows the 11-year running average of near-surface temperature over the land region of South China from 1951 to 2050, with the historical period defined as 1951 to 2000 and the near-future period as 2001 to 2050. Near-surface temperature is projected to increase by about 2 K from 299 K in 1951 to 301 K in 2050, with a much faster trend in the near-future era than in the historical era. In particular, there is only ~0.5 K enhancement of near-surface temperature during the historical era, but ~1.5 K increase in the near-future era. Fig. 3b gives the distribution of 2 m-T difference between near-future and historical era for MJJAS. Strong temperature rise is found over central China, North India, and Mongolia, while the increase of temperature over South China is relatively mild, with warming by about 0.9 to 1.2 K (see the red box).

For daily rainfall, Fig. 4 gives the (a) Simple Day Intensity Index for Rain (SDII) (accumulated rainfall averaged by number of wet days that daily rainfall is larger than 0.1 mm/day) and (b) 95% threshold (R95P) of wet days rainfall difference between near-future and historical era for MJJAS based on GFDL-ESM2M historical and RCP.5 simulation. SDII increases slightly over South China with magnitude of about 0.3 to 0.5 mm/day. The magnitude of extreme rainfall increases by >4 mm/day in parts of South China, and by

Table 1
Values of UCM parameters prescribed for three types of urban categories.

UCM parameter	Type1	Type2	Type3
Anthropogenic heat [W m^{-2}]	15.0	50.0	200.0
Building height [m]	13.31	14.01	53.92
Urban fraction	0.4	0.9	0.7
Standard Deviation of roof height [m]	10.42	5.64	33.18
Roof width [m]	38.01	14.28	35.5
Road width [m]	22.98	13.91	29.6
Surface albedo of road	0.2	0.17	0.18
Surface albedo of roof	0.142	0.165	0.115
Surface albedo of building wall	0.208	0.2	0.22

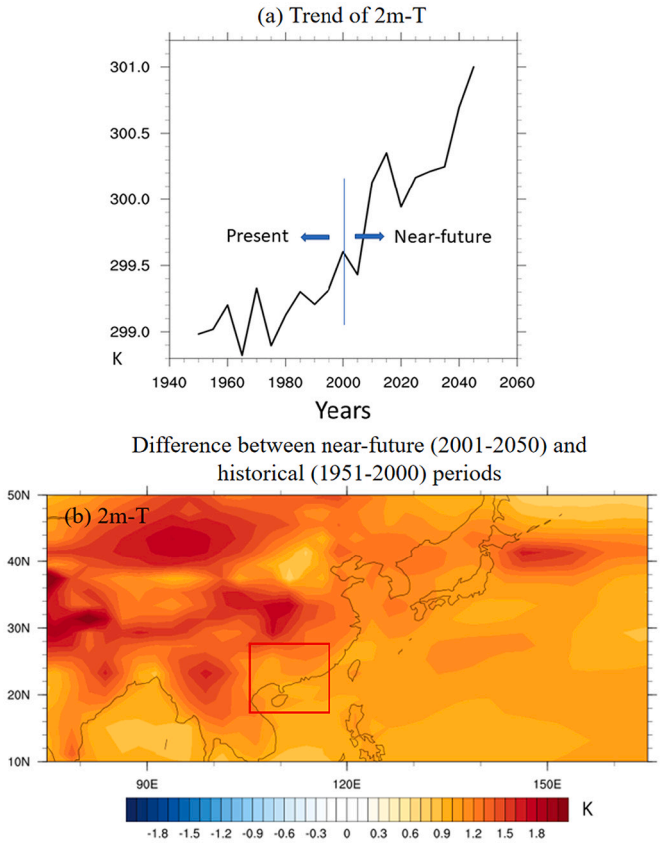

Fig. 3. (a) 2 m temperature (units: K) from historical (1951–2000) to near-future (2001–2050) in summer (MJJAS) over the South China land area, based on GFDL-ESM2M historical and RCP8.5 simulations. (b) 2 m-T difference between historical (1951–2000) and near-future (2001–2050) in summer (MJJAS). The red box marked the South China region (17°-27°N,105°-117°E). (For interpretation of the references to colour in this figure legend, the reader is referred to the web version of this article.)

around 2.5 to 3 mm/day over the GBA area. Overall, the South China 2 m temperature and the 99th percentile of wet days' daily rainfall increase from 299.12 to 300.17 K, and 22.6 to 25.1 mm/day, respectively, in the near future (2001–2050 vs 1950–2000). It is also noteworthy that the number of wet days is expected to decline slightly from 137.34 days/year to 132.7 days/year under global warming. In other words, in a warmer climate, rainfall in GBA would become more intense, while the rain period would decrease.

3.2. Urban development and global warming impact on urban extreme hourly rainfall

The impacts of urban development and global warming on the GBA urban extreme hourly rainfall were examined in the innermost model domain (D03) of WRF outputs. We first investigate the change of surface temperature induced by urban development from 1999 to 2030 over the GBA area, as well as that due to global warming over a comparable period. Fig. 5a compares the hourly 2-m temperature probability density function (PDF) in the range of 17 to 37 °C, based on data aggregated over the GBA urban locations, from the 99LS-HIS, 99LS-FUT, and 30LS-FUT runs. Comparing 99LS-FUT and 99LS-HIS, global warming enhances the urban 2-m temperature substantially, and the frequency of high temperature increases for values larger than 27 °C. For instance, the likelihood of temperature in the range of 28-29 °C increases from 10% to 13%, and the location of maximum PDF shifts to higher values (from 26 to 27 °C to 27-28 °C) in the near future, implying that the probability of higher temperature increases over the urban area under the near-future climate. At the same time, urbanization can also lead to a warmer city environment. Comparing the 30LS-FUT and 99LS-FUT results, the probability of high temperature is further increased due to urban development, with the strongest increment found in the range of 28-29 °C (with probability enhancement from 13% to 15%). Fig. 5 are the 2-m temperature results of 30LS-FUT minus 99LS-HIS, and 30LS-FUT minus 99LS-FUT, averaged over all extreme cases in the GBA region. Overall, urban development can lead to surface warming by about 0.6 to 0.8 °C over the city area. When the effect of global warming is also considered, the 2-m temperature rises by >1 °C in the same region, as compared to 0.6 °C rise over the ocean (see Fig. S3a for the global warming effect only, 99LS-FUT vs 99LS-HIS). Therefore, according to these experiments, global warming and urban development can result in a comparable temperature increase over the GBA mega-urban in the near future.

In order to investigate the influence of urban development and climate change on rainfall characteristics over the GBA mega-city, Fig. 6 shows the mean rainfall difference between (a) 30LS-FUT and 99LS-HIS, and that between (b)30LS-FUT and 99LS-FUT, averaged

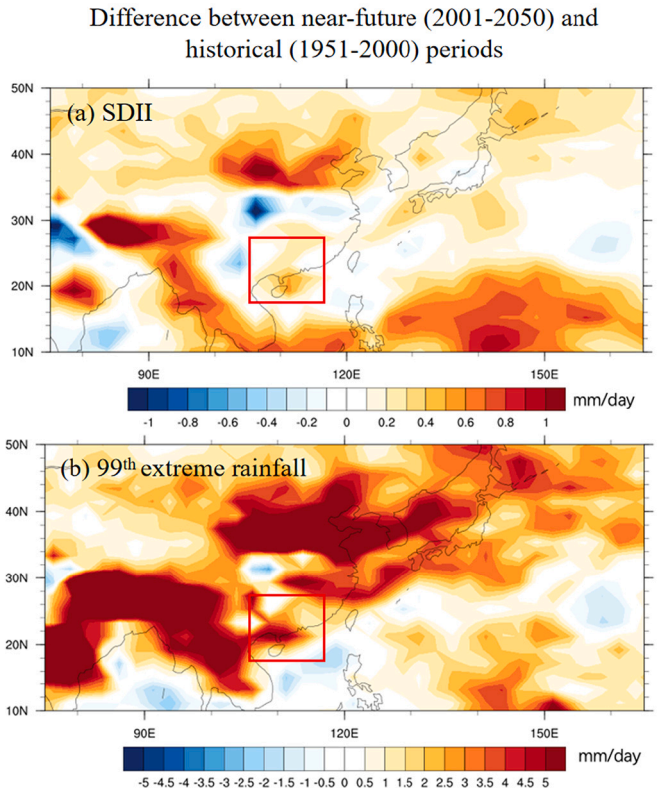

Fig. 4. Horizontal distribution of (a) SDII, (b) 99th wet days extreme rainfall difference between historical (1951–2000) and near-future (2001–2050) in summer (MJJAS), based on GFDL-ESM2M historical and RCP8.5 simulations. The red box marked the South China region (17°-27°N,105°-117°E). (For interpretation of the references to colour in this figure legend, the reader is referred to the web version of this article.)

over on all extreme cases considered. In the near future, the mean rainfall amount over the GBA urban area, for these extreme events, is enhanced by about 5–8 mm/day over part of the land area due to global warming, but the difference in rainfall intensity can be much smaller in the coastal area (see Fig. S3b). Future projected urban development also leads to more accumulated rainfall, but only at highly urbanized locations (the GBA city cluster comprising Guangzhou, Foshan, and Dongguan, between 113.2 and 113.7°E, 22.8 to 23.3°N; see open green circles in Fig. 6b), with significant enhancement by about 8–10 mm/day. Over the more southern part of the domain, rainfall change seems to be insignificant, which might be related to the weaker changes of temperature and vertical motion. When considering the whole 2030 GBA urban area, the area averaged accumulated rainfall increased by about 13.5% due to global warming; and the increment is about 9.7% due to the projected urban development alone. Student's *t*-test is conducted to examine the statistical significance of changes in rainfall characteristics (see black dots in Fig. 6a and b). Statistical tests confirm that the aforementioned precipitation change over land in the northeast/west part of the domain, due to global warming in near future, passes the 95% significance level. Increased total rainfall in the north part of the megacity area, caused by projected urban development, is also found to be statistically significant.

For the rainfall frequency, PDFs of hourly precipitation rates over the mega-urban area are considered. Fig. 6c shows rainfall PDFs from 99LS-HIS, 99LS-FUT, and 30LS-FUT experiments within the range of 1 to 110 mm/h. Compared with 99LS-HIS, the frequency of light rainfall events (those from 1 to 10 mm/h) for 99LS-FUT is decreased (by about 20% or more). On the other hand, global warming can strongly increase the probability of heavy rainfall (>50 mm/h) in the near future, with the likelihood enhanced by about 30 to 80%. By comparing 99LS-FUT and 30LS-FUT, it can be inferred that urban development can also enhance the probability of urban hourly precipitation; however, such enhancement is found for all rain rates (1-110 mm/h), with even stronger effect on heavy rainfall (i.e., rain rate >50 mm/h). Due to GBA urban development, the frequency of hourly rainfall in the range of 50-100 mm/h increases by about 40 to 80%. It is noteworthy that both urban development and global warming can enhance the frequency and intensity of extreme rainfall over the GBA urban area.

To better compare impacts of urban development and global warming on rainfall frequency, Fig. 6d shows the ratio of rainfall probability between 30LS-FUT and 99LS-HIS (black), 99LS-FUT and 99LS-HIS (blue), and 30LS-FUT and 99LS-FUT (red) over the region with strongest signals in the Pearl River Estuary area (see black box in Fig. 6a and b). When considering both urban development and global warming (see 30LS-FUT vs 99LS-HIS curve), jointly they have much stronger impacts on probability of heavy rainfall occurrence than that of light rainfall; the probability of rainfall larger than 50 mm/h is more than doubled, but increment is <50% for hourly rainfall events weaker than 30 mm/h. It is noteworthy that urban development seems to have stronger influence on

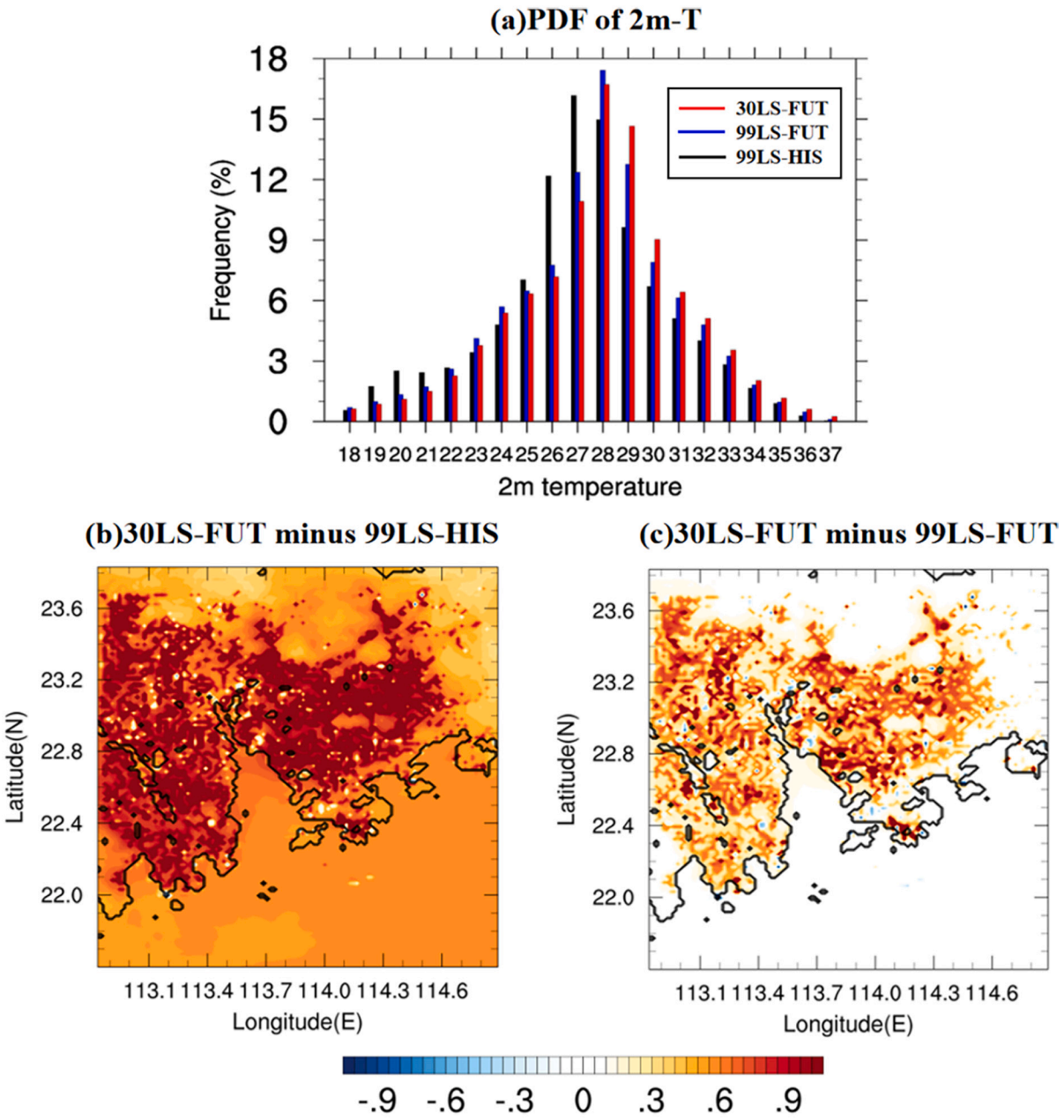

Fig. 5. (a) PDFs of hourly 2 m temperature within the range of 17-37 °C for the 99LS-HIS (black), 99LS-FUT (blue), 30LS-FUT (red) experiments over corresponding urban locations within GBA (all urban grids in 1999 or 2030 land use). (b) 2 m temperature difference (units:°C) between (b) 99LS-HIS and 30LS-FUT and (c) 99LS-FUT and 30LS-FUT. Temperatures are computed by averaging over entire integrations for all selected extreme cases. See text for details. The coastline is shown by black line. (For interpretation of the references to colour in this figure legend, the reader is referred to the web version of this article.)

extremely intense rainfall; the probability of precipitation larger than 90 mm/h is doubled as a result of urban development (see 30LS-FUT vs 99LS-FUT). On the other hand, the global warming effect is most prominent within the range of 40-60 mm/h, with frequency enhanced by about 80 to 100% (see 99LS-FUT vs 99LS-FUT). Finally, we believe that compared to global warming under RCP8.5 scenario, the near-future projected urban development has a comparable effect on both near-surface temperature and extreme precipitation over the GBA mega-urban area.

Moreover, according to the CC relationship, the saturated vapor pressure increases by ~7% per degree warming in low-level temperature. Based on GFDL-ESM2M data, the GCM runs are considered to give 1.1 °C warming from 1951 to 2000 to 2001–2050, while the 95th percentile of daily rainfall intensity increases by about 7.4% over the GBA. When comparing 99LS-FUT vs 99LS-HIS

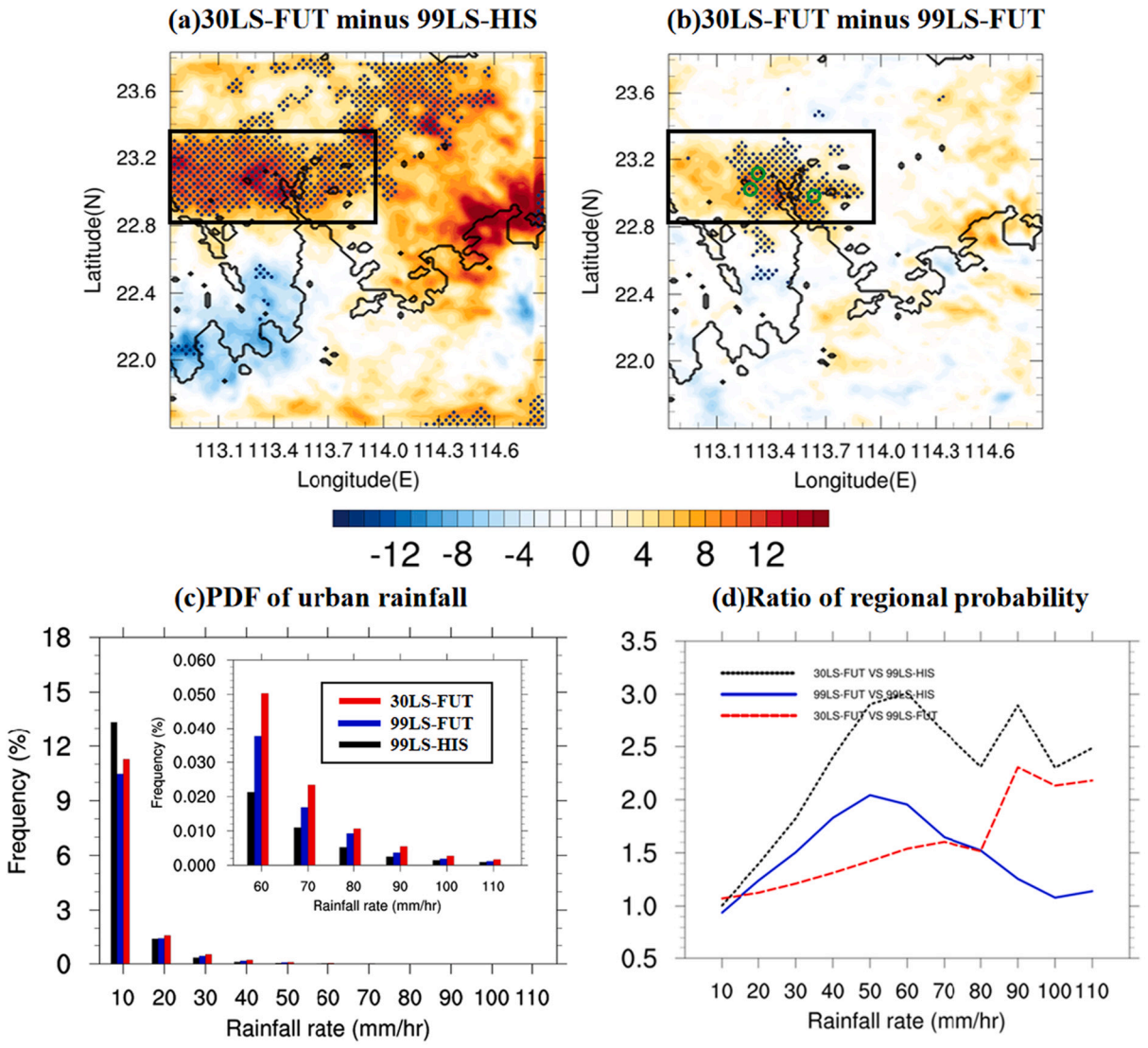

Fig. 6. (a), (b) Same as Fig. 5b, and c except for daily accumulated rainfall (units: mm/day), averaged over entire integrations for all selected extreme cases, with green circles indicating the locations, from west to east, of Foshan, Guangzhou, and Dongguan. Locations in which the difference exceeds the 95% significance level are denoted by black dots. (c) PDFs of hourly precipitation rates within the ranges of 1–10, 10–20, 20–30, 30–40, 40–50, 50–60, 60–70, 70–80, 80–90, 90–100, and 100–110 mm/h (denoted by the labels 10, 20, 30, 40, 50, 60, 70, 80, 90, 100, 110 mm/h, respectively) for the 99LS-HIS (black), 99LS-FUT (blue), 30LS-FUT (red) experiments over corresponding urban locations within GBA (i.e., all urban grids for 1999 or 2030 land use). (d) Ratio of hourly rain rate probability between 30LS-FUT and 99LS-HIS (black), 99LS-FUT and 99LS-HIS (blue), and 30LS-FUT and 99LS-FUT (red) within the ranges of 1-110 mm/h, based on hourly rainfall data within the black box region in Fig. 3a and b. (For interpretation of the references to colour in this figure legend, the reader is referred to the web version of this article.)

innermost domain averaged 95th percentile hourly rainfall for all cases, similar scaling is found (approximately 7.9%/K warming) in our dynamical-downscaling results.

3.3. *Mechanism of urban and global warming impacts*

To understand the mechanism that why urban development and global warming have a positive impact on both frequency and intensity of GBA mega-urban extreme rainfall. Fig. 7 shows the (a) surface evaporation and (b) precipitable water difference (units: g/m^2/s) between 99LS-FUT and 99LS-HIS, computed by averaging over entire integrations for all selected extreme cases. In fact, warmer climate results in more surface evaporation, which increases the background moisture content. Such enhanced evaporation leads to increased precipitable water in 99LS-FUT than in 99LS-HIS across the whole GBA region (see Fig. 7b), which is conducive to more intense extreme rainfall in the near future.

The convective available potential energy (CAPE) and convective inhibition (CIN) are also considered. Fig. 8 gives the vertical profiles of CAPE and CIN with parcels rising in various levels, averaged over the urban area from 99LS-FUT and 99LS-HIS. Global warming results in a decrease of CAPE from the surface to 600 m of height. But there is a stronger increase in CAPE for air parcels above 600 m, reaching 43 J/kg at 1000 m, implying stronger convection and vertical motion. However, under a warmer climate, the CIN also increases from 400 to 1400 m, leading to a more stable atmosphere. That can be attributed to that temperature and relative humidity difference caused by warmer background climate (99LS-FUT vs 99LS-HIS) increases with height, while the area mean temperature (relative humidity) difference in the urban is only about 0.4 °C (0.57%) at surface, increasing to 0.75 °C (1.04%) at 2000 m (see fig. S4). Hence, the 99LS-FUT experiment produces higher environment virtual temperature, leading to increased CIN for air parcels under 1400 m when compared to the 99LS-HIS experiment. This is consistent with the findings that global warming can enhance thermal stability and make convection more difficult to be triggered (Chou et al., 2012; Hsu et al., 2012; Dai et al., 2017; Chou and Neelin, 2004; Kenshi et al., 2018). The increased precipitable water and atmospheric stability play an opposite effect on extreme rainfall. When it comes to these extreme precipitation events, more intense and frequent extreme rainfall over land areas could be caused by increased moisture content under a warmer climate, while the GBA mega-urban area's lower frequency of light rainfall (1 to 10 mm/h) in 99LS-FUT is probably caused by the higher CIN.

On the other hand, urbanization (change of surface land use) is known to cause reduced surface humidity over the urban area due to decreased surface evaporation, which leads to a decrease of CAPE for parcel under 600 m of height. However, the CAPE difference is weak above 600 m (no >3 J/kg) over the 2030 GBA megacity. Considering that urban development's effects are not homogeneous over the whole city area, the CAPE difference for parcels rising at 1000 m between 30LS-FUT and 99LS-FUT is calculated (see Fig. S5). CAPE increases by about 15 to 40 J/kg over north and northwest parts of the mega urban region (again locations with the greatest urban development, such as Guangzhou, Dongguan, Foshan, and Panyu, indicated by pen green circles in Fig. S5), which strengthen local convection on these locations. The enhanced CAPE is also consistent with the rainfall increase (about 3-12 mm/d) at the same locations.

To find out whether urban development affects convection and local water vapor content, Fig. 9 gives the vertical profiles of specific humidity and wind difference between 30LS-FUT and 99LS-FUT along a northeast-southwest (45°) cross section (see Fig. 2c). At the bottom of the same figure, red and blue bars indicate the projected new urban area in 2030 and the existing urban area in 1999, respectively. Due to urban development, more water vapor is found at the height from 300 m to 6 km, which can be attributed to increased moisture flux convergence in relation to induced circulation by a stronger UHI effect, especially in the highly urbanized megacity area (such as Dongguan), with specific humidity increased >0.15 g/kg from 500 m to 5 km. Compared with the 99LS-FUT experiment, 30LS-FUT gives stronger vertical motion over the most urban area from 1 km to 6 km. This is especially the case over the highly urbanized region of 113.2 to 114.2°E, with obvious development in 2030 compared to 1999. Similar results are found for other cross-sectional plots. The east-west cross-section through Guangzhou (see Fig. S6a) shows enhanced specific humidity and vertical motion over the Guangzhou and Foshan area, with anomalous enhanced specific humidity reaching 5 km in the highly urbanized area, consistent with stronger vertical motion there. According to the south-to-north cross-section through Guangzhou (see Fig. S6c), urban

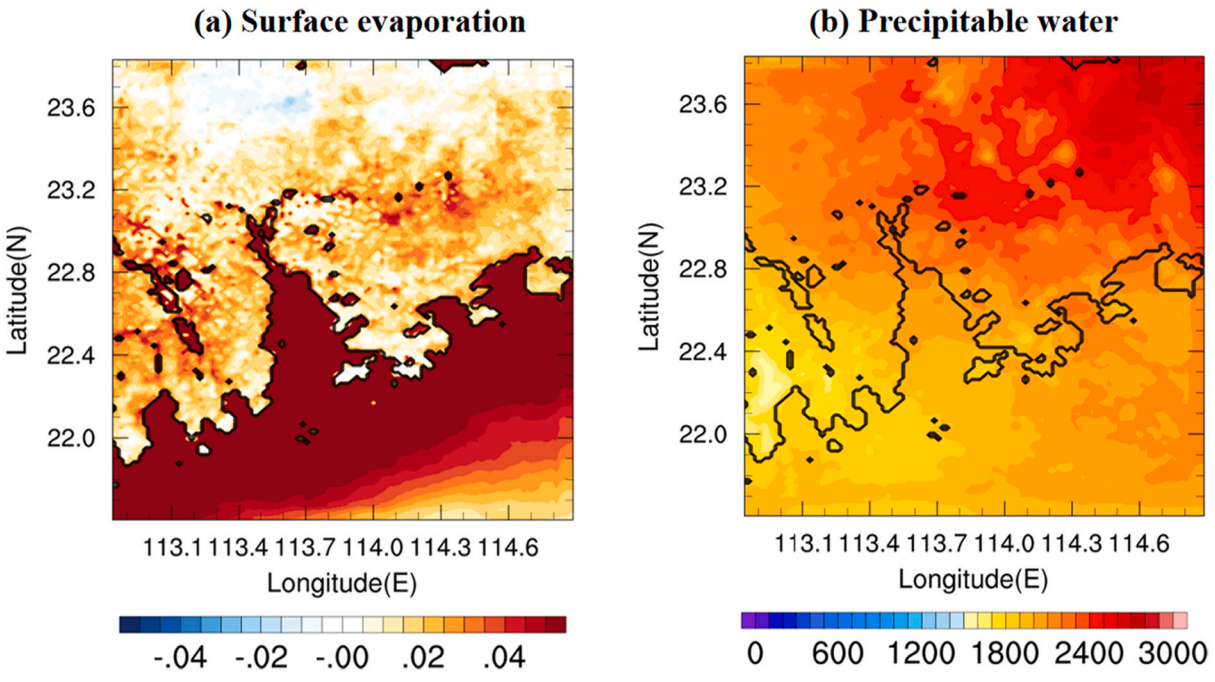

Fig. 7. (a) Surface evaporation (units: g/m^2/s) and (b) Precipitable water (units: g/m^2) difference between 99LS-FUT and 99LS-HIS, computed by averaging over entire integrations for all selected extreme cases.

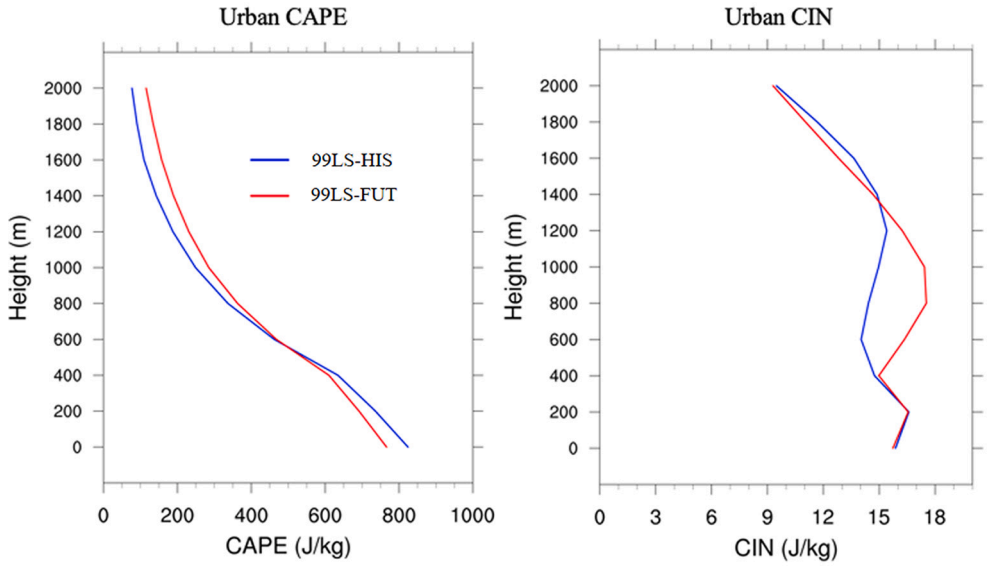

Fig. 8. (a)Vertical CAPE profile averaged over urban grids in d03 from 99LS-HIS (blue) and 99LS-FUT (red). CAPE is computed by averaging over entire integrations for all selected extreme cases. (b) Same as (a) except for CIN. (For interpretation of the references to colour in this figure legend, the reader is referred to the web version of this article.)

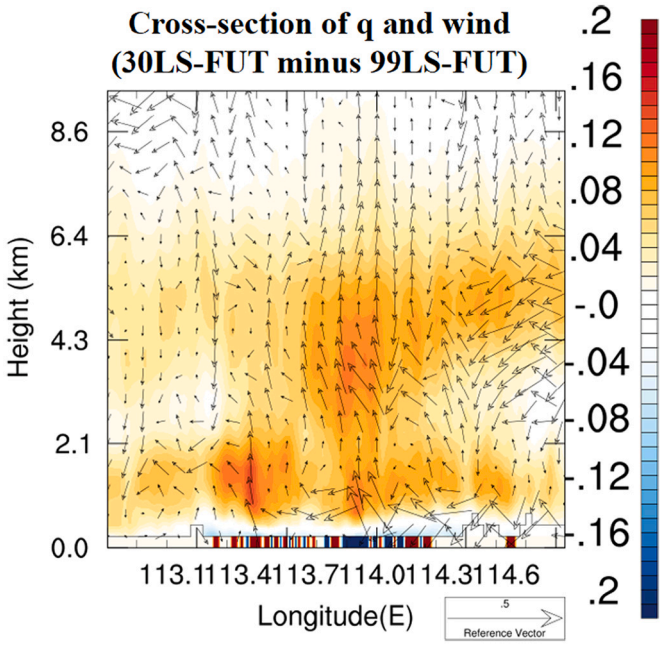

Fig. 9. Cross section of difference of hourly vertical wind vector (units: m/s) and specific humidity (units: g/kg), averaged over all cases during their entire integration, between 99LS-FUT and 30LS-FUT, with blue bar representing the urban area in 1999 and red bar newly developed urban area in 2030. (For interpretation of the references to colour in this figure legend, the reader is referred to the web version of this article.)

development and presumably the induced additional UHI can lead to anomalous low-level southerly flow from the ocean toward the city area, advecting moisture into the mega-urban region which further support the enhanced extreme rainfall.

Moreover, compared with GBA urban land use in 1999 and 2030, large changes of urban development were found in two regions between 22.9 and 23.2 N, 113.0–113.4E (Guangzhou and Foshan) and 22.5–22.8 N, 113.8–114.3E (Shenzhen and Hong Kong) (see Fig. 2b and c), while enhanced precipitation and CAPE were only found in the former region due to urban development. For the latter region, there are also stronger low-level southerly flow and slightly enhanced water vapor above 500 m due to urban development (see Fig. S6e). However, the change of vertical wind speed is weak over Hong Kong and Shenzhen; there is even decreased vertical wind

speed above 3 km over 22.6–22.8 N due to urban development. It appears that due to the strongly enhanced vertical motion over Guangzhou, Foshan, and Dongguan (the former region with rapidly urban development), the sinking branch from the north and northwest part of the domain tends to suppress convection over other urban locations (such as Shenzhen and Hong Kong, 22.5–22.8 N, 113.8–114.3E). Hence stronger convection and precipitation are only found in the north and northwest part of the megacity. Overall, the 30LS-FUT experiment shows that urban development can influence local circulation and convection over some highly urbanized areas. Stronger convection found over the area with strongest urban development is consistent with higher CAPE over the same locations. In addition, induced low-level convergence and southerly flow from the ocean act to increase the atmospheric moisture content, which is also conducive to stronger and more frequent extreme rainfall there.

4. Discussions and summary

In this study, impact of near-future urban development on hourly extreme rainfall projection over the GBA mega-urban region has been investigated and compared with global warming effect, based on dynamical downscaling of extreme rainfall cases taken from GCM runs using a convection-permitting regional model, with three types of urban land use and corresponding parameters incorporated in the model's urban canopy. Parallel experiments were designed by varying the urban land use (1999 vs 2030) and background climate conditions (historical vs near-future). Results showed that urban development can lead to surface warming by about 0.6 to 0.8 °C over the city area. Surface temperatures across the GBA land (nearby ocean) could increase by ~0.3 to 0.8 °C (0.4 to 0.8 °C) in the near-future global warming. For precipitation, both urban development and global warming can enhance the intensity as well as the occurrence rate of extreme rainfall. Global warming can increase the extreme rainfall amount (averaged over entire integrations for all selected extreme cases) over part of the GBA land area by about 3-12 mm/day, while the increase due to urban development was found to be around 6–12 mm/day over the north and northwest part of GBA region (i.e. locations which are projected to become even more urbanized in the near future). Moreover, the intensity of accumulated rainfall averaged over the 2030 GBA urban area increased by about 13.5% (9.7%) due to global warming (urban development). This result is consistent with a recent meta-data analysis which reported that accumulated rainfall increases by about 11 to 21% in the city center (and 14 to 22% in the downwind direction) due to urbanization (Liu and Niyogi, 2019). Results also show that the increased extreme rainfall over the GBA region in both GCM data and dynamical downscaling outputs owing to global warming is followed the CC relationship (with the 95th percentile hourly rainfall increasing by about 7.9%/K warming in the innermost model domain).

It was also found that, due to the multi-center nature of GBA mega-city, sinking branch from the highly urbanized area could suppress convection over the urban in coastal areas (such as Shenzhen). Hence stronger convection and precipitation were only found in north and northwest parts of the domain. Note that global warming reduces the frequency of light rainfall (by around 20%) during these extreme precipitation events, which may be attributed to stronger CIN and more stable atmosphere in a warmer climate. But for heavy rainfall (within the range of 40 to 60 mm/h), global warming would substantially enhance its probability by about 1.3 to 1.8 times, which is supported by the enhanced evaporation and water vapor in the atmosphere under a warmer climate. In contrast, urban development can increase the likelihood of urban rainfall in all ranges (1-110 mm/h). Fractional increase of probability from 99LS-FUT to 30LS-FUT is <5% for light rainfall (1–10 mm/h), but reaching 40 to 80% for heavy rainfall (50-110 mm/h), especially extremely heavy rainfall (stronger than 90 mm/h). Significant increase in extreme rain rates is due to regionally increased CAPE as well as decrease in CIN, resulting in stronger local convection and vertical motion in some highly urbanized areas. The ocean also has an important effect versus urbanization on rainfall in the coastal GBA. Though urban development can reduce near-surface water vapor content on the large scale (30LS-FUT vs 99LS-FUT), urban development still results in more water vapor above the height of 300 m during extreme rainfall events because of stronger induced low-level southerly flow (from the ocean to megacity area) and stronger moisture flux convergence. Overall, it is found that incorporating future urban development information is of great importance for the GBA region, in view of comparable impacts on temperature, intensity and frequency of extreme rainfall over the GBA mega-urban area compared to the near-future global warming forcing.

There are some limitations in this study. It is known that urban-induced aerosol can have a cooling effect and inhibit the formation of rainfall in some situations. However, aerosols and their future changes are not considered; their impacts on urban extreme rainfall will be researched in future studies. Moreover, this study only explores extreme rainfall cases from only one GCM (GFDL-ESM2M). We suspect the effect of urban development is not too sensitive to the background climate. Under other GCM climate conditions, higher surface temperature and more moisture flux convergence induced by urban development can still enhance the intensity and frequency of precipitation over the GBA mega-urban area. Further examination of global warming signals revealed that increase in SST and evaporation provided by GFDL-ESM2M are generally consistent with other GCM projections. Still, it will be interesting to dynamically downscale products from other GCMs, using the same regional modeling framework, to further compare the impacts of urbanization vs global warming on severe rainfall over GBA or other coastal mega-cities.

Finally, the urban canopy model used here only incorporates three types of urban land use for simplifying the simulations and decreasing model uncertainties. But such representation may still not be realistic enough for a complex urban environment, such as that of the GBA mega-urban cluster. Details such as heat released by air conditioning and its timing, interaction with various atmospheric layers, and so on are neglected. In our next study, we intend to adopt a multi-layer urban canopy module that allows more urban land types, with parameters based on the World Urban Database and Access Portal Tools (WUDAPT) dataset (Ching et al., 2018; Wang et al., 2019). Such a modeling system will be ideal for studying the interaction between realistic urban environments and mesoscale systems. Results should be invaluable for mitigating and adapting to extreme weather and related hazards that occur in highly urbanized locales, such as urban flooding (compounded by the effect of impervious surfaces (Blum et al., 2020)), under the present as well as the future climate.

Author contribution

All authors contributed to Conceptualization, and Writing-original draft. C.-Y. T. contributed to Methodology, Project administration, Funding acquisition, and Supervision. C. H. carried out Formal analysis, Methodology, Investigation, and Writing - review & editing. C. H., Z. W., and C.-Y. T. prepared the main Writing - original draft. C. H., X. L., C. R., K. H., and K. F. provided the Data curation

Author statement

The authors declare all authors have seen and approved the manuscript being submitted and the article is the authors' original work, hasn't received prior publication and isn't under consideration for publication elsewhere.

Declaration of Competing Interest

The authors declare no competing financial interests.

Data availability

Data will be made available on request.

Acknowledgments

We thank Drs. Ruby Leung, Zong-Liang Yang for discussions. This work is jointly supported by the National Key Research and Development Program of China (Ref. No. 2019YFC1510400), the Hong Kong Research Grant Council's General Research Fund (Ref. No. 14308017), Research Impact Fund 2018-19 (Ref. No. R4046-18, named 'Increasing the Resilience to the Health Impacts of Extreme Weather on Older People under Future Climate Change'), and Shenzhen Research Institute, the Chinese University of Hong Kong (Grant No. A.02.20.00401). High performance computation was supported by Information Technology Services Centre of the Chinese University of Hong Kong. All raw data utilized in this study is publicly accessible in the following ways. The GFDL-ESM2M data were from this website- ftp://nomads.gfdl.noaa.gov/CMIP5/output1/NOAA-GFDL/GFDL-ESM2M/. The Weather research and forecasting (WRF) model V3.8.1 coupled with single layer urban canopy model (SLUCM) was downloaded online (https://www2.mmm.ucar.edu/wrf/users/download/get_sources.html). ERA-Interim was from https://www.ecmwf.int/en/forecasts/datasets/. TRMM-3B42 rainfall estimate products are from https://doi.org/10.5067/TRMM/TMPA/3H/7. Station-based APHRODITE land precipitation data are from http://aphrodite.st.hirosaki-u.ac.jp/download/. Variables from WRF model output are available on Zenodo (http://doi.org/10.5281/zenodo.4892887).

Appendix A. Supplementary data

Supplementary data to this article can be found online at https://doi.org/10.1016/j.uclim.2022.101389.

References

Baik, J., Kim, Y., Chun, H., 2001. Dry and moist convection forced by an urban Heat Island. J. Appl. Meteorol. 40 (8), 1462–1475.
Blum, A., Ferraro, P., Archfield, S., Ryberg, K., 2020. Causal effect of impervious cover on annual flood magnitude for the United States. Geophys. Res. Lett. 47 (5).
Bornstein, R., 1968. Observation of the urban Heat Island effect in New York City. J. Appl. Meteorol 7 (4), 575–582.
Bougeault, P., Lacarrere, P., 1989. Parameterization of orography-induced turbulence in a Mesobeta-scale model. Mon. Weather Rev. 117, 1872–1890.
Chang, C., Lei, Y., Sui, C., Lin, X., Ren, F., 2012. Tropical cyclone and extreme rainfall trends in east Asian summer monsoon since mid-20th century. Geophys. Res. Lett. 39 (18).
Changnon, S., 1968. The La Porte weather anomaly—fact or fiction? Bull. Am. Meteorol. Soc. 49 (1), 4–11.
Chen, H., 2013. Projected change in extreme rainfall events in China by the end of the 21st century using CMIP5 models. Chin. Sci. Bull. 58 (12), 1–10.
Chen, F., Dudhia, J., 2001. Coupling and advanced land surface-hydrology model with the Penn State-NCAR MM5 modeling system. Part I: model implementation and sensitivity. Mon. Weather Rev. 129 (4), 569–585.
Chen, Y., Li, X., Liu, X., Ai, B., 2014. Modeling urban land-use dynamics in a fast developing city using the modified logistic cellular automaton with a patch-based simulation strategy. Int. J. Geogr. Inf. Sci. 28, 234–255.
Ching, J., Mills, G., el al., 2018. WUDAPT: an urban weather, climate, and environmental modeling infrastructure for the Anthropocene: WUDAPT is an international community-generated urban canopy information and modeling infrastructure to facilitate urban-focused climate, weather, air quality, and energy-use modeling application studies. Bull. Am. Meteorol. Soc. 99 (9), 1907–1924.
Chou, C., Neelin, J., 2004. Mechanisms of global warming impacts on regional tropical precipitation. J. Clim. 17 (13), 2688–2701.
Chou, C., Chen, C., Tan, P., Chen, K., 2012. Mechanisms for global warming impacts on precipitation frequency and intensity. J. Clim. 25 (9), 3291–3306.
Dai, A., Rasmussen, R., Liu, C., Ikeda, K., Prein, A., 2017. A new mechanism for warm-season precipitation response to global warming based on convection-permitting simulations. Clim. Dyn. 55 (1–2), 1–26.
Dee, D., Uppala, S., Simmons, A., Berrisford, P., Poli, S., Kobayashi, U., et al., 2011. The ERA-interim reanalysis: configuration and performance of the data assimilation system. Q. J. R. Meteorol. Soc. 137 (656), 553–597.
Dou, J., Wang, Y., Bornstein, R., Miao, S., 2015. Observed spatial characteristics of Beijing urban climate impacts on summer thunderstorms. J. Appl. Meteorol. Climatol. 54 (1), 94–105.

Dudhia, J., 1989. Numerical study of convection observed during the winter monsoon experiment using a mesoscale two-dimensional model. J. Atmos. Sci. 46, 3077–3107.
Dunne, J., John, J., Adcroft, A., Griffies, S., Hallberg, R., Shevliakova, E., et al., 2012. GFDL's ESM2 global coupled climate–carbon earth system models. Part I physical formulation and baseline simulation characteristics. J. Clim. 25 (19), 6646–6665.
Dunne, J., Jasmin, G., John, E., Shevliakova, E., Ronald, J., et al., 2013. GFDL's ESM2 global coupled climate-carbon earth system models. Part II: carbon system formulation and baseline simulation characteristics. J. Clim. 26 (7), 2247–2267.
Fan, Yifan, Li, Yuguo, Yin, Shi, 2018. Interaction of multiple urban heat island circulations under idealised settings. Build. Environ. 134, 10–20.
Fung, K., Tam, C., Chinese University of Hong Kong, 2018. Comparing the Urban Heat and Global Warming Impacts on Extreme Rainfall Characteristics in Pearl River Delta Based on Dynamical Downscaling. Graduate School. Division of Earth Atmospheric Sciences.
Fung, K.Y., Tam, C.-Y., Lee, T.C., Wang, Z., 2021. Comparing the anthropogenic heat and global warming impacts on extreme precipitation in urbanized Pearl River Delta area based on dynamical downscaling. J. Geophys. Res. 126, 21.
Guo, X., Fu, D., Wang, J., 2006. Mesoscale convective precipitation system modified by urbanization in Beijing city. Atmos. Res. 82, 112–126.
Han, J., Baik, J., 2008. A theoretical and numerical study of urban heat island-induced circulation and convection. J. Atmos. Sci. 65 (6), 1859–1877.
Han, J., Pan, H., 2011. Revision of convection and vertical diffusion schemes in the NCEP global forecast system. Weather Forecast. 26 (4), 520–533.
Han, J., Baik, J., Lee, H., 2014. Urban impacts on precipitation. Asia-Pac. J. Atmos. Sci. 50 (1), 17–30.
Hannah, R., 2018. Urbanization. Published online at OurWorldInData.org. Retrieved from "https://ourworldindata.org/urbanization".
Holst, C.C., Tam, C., Chan, J., 2016. Sensitivity of urban rainfall to anthropogenic heat flux: a numerical experiment. Geophys. Res. Lett. 43 (5), 2240–2248.
Holst, C., Chan, J., Tam, C.-Y., 2017. Sensitivity of precipitation statistics to urban growth in a subtropical coastal megacity cluster. J. Environ. Sci. 59, 6–12.
Hong, S., Lim, J., 2006. The WRF single-moment 6-class microphysics scheme (WSM6). J. Korean Meteorol. Soc. 42 (2), 129–151.
Hsu, P., Li, T., Luo, J., Murakami, H., Kitoh, A., Zhao, M., 2012. Increase of global monsoon area and precipitation under global warming: a robust signal? Geophys. Res. Lett. 39 (6).
Hu, C., Fung, K., Tam, C.-Y., Wang, Z., 2021. Urbanization impacts on Pearl River Delta extreme rainfall – sensitivity to land cover change vs anthropogenic heat. Earth Space Sci 8 (3).
Huang, K., Leng, J., Xu, Y., Li, X., Cai, M., Wang, R., Ren, C., 2021. Facilitating urban climate forecasts in rapidly urbanizing regions with land-use change modeling. Urban Clim. 36, 100806.
Huff, F., Changnon, S., 1972. Climatological assessment of urban effects on precipitation at St. Louis. J. Appl. Meteorol. 11 (5), 823–842.
Huffman, G., Stocker, D., Bolvin, E., Nelkin., 2014. TRMM 3B42 Precipitation Data Set. NASA Goddard Space Flight Center.
Iacono, M., Delamere, J., Mlawer, E., Shephard, M., Clough, S., Collins, W., 2008. Radiative forcing by long-lived greenhouse gases: calculations with the AER radiative transfer models. J. Geophys. Res.-Atmos. 113 (D13).
Iwashima, T., Yamamoto, R., 1993. A statistical analysis of the extreme events: long-term trend of heavy daily precipitation. J. Meteorol. Soc. Jpn. 71 (5), 637–640.
Janjic, Z.I., 2002. Nonsingular implementation of the Mellor-Yamada level 2.5 scheme in the NCEP Meso model. NCEP Office Note No. 437, 61 pp.
Karl, T., Knight, R., 1998. Secular trends of precipitation amount, frequency, and intensity in the USA. Bull. Am. Meteorol. Soc. 79, 231–241.
Kenshi, H., Izuru, T., Yasutaka, W., Tomomichi, O., 2018. Physical responses of convective heavy rainfall to future warming condition: case study of the Hiroshima event. Front. Earth Sci. (Lausanne) 6, 2018-04-19.
Kharin, V., Zwiers, F., Zhang, X., Hegerl, G., 2007. Changes in temperature and precipitation extremes in the IPCC ensemble of global coupled model simulations. J. Clim. 20 (8), 1419–1444.
Knutson, T.R., Kossin, J.P., Mears, C., et al., 2017. Detection and attribution of climate change. In: Wuebbles, D.J., Fahey, D.W., Hibbard, K.A., et al. (Eds.), Climate Science Special Report: Fourth National Climate Assessment, Volume I. U. S. Global Change Research Program, Washington, DC, USA, pp. 114–132.
Kusaka, H., Kimura, F., 2004. Thermal effects of urban canyon structure on the nocturnal Heat Island: numerical experiment using a mesoscale model coupled with an urban canopy model. J. Appl. Meteorol. 43 (12), 1899–1910.
Kusaka, H., Nawata, K., Suzuki-Parker, A., Takane, Y., Furuhashi, N., 2014. Mechanism of precipitation increase with urbanization in Tokyo as revealed by ensemble climate simulations. J. Appl. Meteorol. Climatol. 53 (4), 824–839.
Li, M., Song, Y., Mao, Z., Liu, M., Huang, X., 2016. Impacts of thermal circulations induced by urbanization on ozone formation in the Pearl River Delta region, China. Atmos. Environ. 127, 382–392.
Lin, C., Chen, W., Liu, S., Liou, Y., Liu, G., Lin, T., 2008. Numerical study of the impact of urbanization on the precipitation over Taiwan. Atmos. Environ. 42 (13), 2934–2947.
Liu, J., Niyogi, D., 2019. Meta-analysis of urbanization impact on rainfall modification. Sci. Rep. 9 (1), 7301.
Liu, X., Liang, X., Li, X., Xu, X., Ou, J., Chen, Y., Li, S., Wang, S., Pei, F., 2017. A future land use simulation model (FLUS) for simulating multiple land use scenarios by coupling human and natural effects. Landsc. Urban Plan. 168, 94–116.
Luo, M., Lau, N.-C., 2017. Heat waves in southern China: synoptic behavior, long-term change and urbanization effects. J. Clim. 30 (2), 703–720.
Marta, M., Jan, K., 2020. Overview of observed Clausius-Clapeyron scaling of extreme precipitation in Midlatitudes. Atmosphere 11 (8), 786.
McSweeney, C.F., Jones, R.G., Lee, R.W., Rowell, D.P., 2015. Selecting CMIP5 GCMs for downscaling over multiple regions. Clim. Dyn. 44 (11−12), 3237–3260.
Meehl, G., Stocker, T., Collins, W., et al., 2007. Global climate projections. In: Solomon, S., Qin, D., Manning, M., Chen, Z., Marquis, M., Averyt, K.B., Tignor, M., Miller, H.L. (Eds.), Climate Change 2007: The Physical Science Basis. Contribution of Working Group I to the Fourth Assessment Report of the Intergovernmental Panel on Climate Change. Cambridge University Press, Cambridge, United Kingdom and New York, NY, USA.
Mohajerani, A., Bakaric, J., Jeffrey-Bailey, T., 2017. The urban heat island effect, its causes, and mitigation, with reference to the thermal properties of asphalt concrete. J. Environ. Manag. 197, 522–538.
Myhre, G., Alterskjaer, K., Stjern, C.W., Hodnebrog, O., Marelle, L., Samset, B.H., et al., 2019. Frequency of extreme precipitation increases extensively with event rareness under global warming. Sci. Rep. 9 (1), 16063–10.
Oke, T., 1988. The urban energy balance. Prog. Phys. Geogr. 12 (491).
Shahmohamadi, P., Che-Ani, A.I., Maulud, K.N.A., Tawil, N.M., Abdullah, N.A.G., 2011. The impact of anthropogenic heat on formation of urban Heat Island and energy consumption balance. Urban Stud. Res. 2011, 1–9.
Shem, W., Shepherd, M., 2009. On the impact of urbanization on summertime thunderstorms in Atlanta: two numerical model case studies. Atmos. Res. 92 (2), 172–189.
Shepherd, J., Burian, S., 2003. Detection of urban-induced rainfall anomalies in a major coastal city. Earth Interact. 7.
Shimadera, H., Kondo, A., Shrestha, K., Kitaoka, K., Inoue, Y., 2015. Numerical evaluation of the impact of urbanization on summertime precipitation in Osaka, Japan. Adv. Meteorol. 2015 (2015), 149–159.
Skamarock, W., Klemp, J., Dudhia, J., Gill, D., Barker, D., Duda, M., Huang, X., Wang, W., Powers, J., 2008. A description of the advanced research WRF version 3 NCAR tech. Note, NCAR/TN–475+STR.
Soltani, A., Sharifi, E., 2017. Daily variation of urban heat island effect and its correlations to urban greenery: a case study of Adelaide. Front. Architect. Res. 6 (4), 529–538.
Stewart, I., Oke, T., 2012. Local Climate Zones for Urban Temperature Studies. Bull. Am. Meteorol. Soc. 93, 1879–1900.
Stewart, I., Oke, T., Krayenhoff, E., 2014. Evaluation of the 'local climate zone' scheme using temperature observations and model simulations. Int. J. Climatol. 34 (4), 1062–1080.
Sun, X., Luo, Y., Gao, X., Wu, M., Li, M., Huang, L., Zhang, D., Xu, H., 2021. On the localized extreme rainfall over the Great Bay Area in South China with complex topography and strong UHI effects. Mon. Weather Rev. 149, 2777–2801.
Tabari, H., 2020. Climate change impact on flood and extreme precipitation increases with water availability. Sci. Rep. 10 (1), 13768.
Tewari, M.F., Chen, F., Kusaka, H., Miao, S., 2008. Coupled WRF/Unified Noah/Urban-Canopy Modeling System. NCAR WRF Documentation. NCAR, Boulder, pp. 1–20.

Wai, M.K., Welsh, T., Ma, W.M., 1995. The timing and distribution of summer convective rainfall over Hong Kong and South China. Hong Kong Meteorol. Soc. Bull. 5 (2).
Wang, D., Jiang, P., Wang, G., Wang, D., 2015. Urban extent enhances extreme precipitation over the Pearl River Delta, China. Atmos. Sci. Lett. 16 (3), 310–317.
Wang, R., Cai, M., Ren, C., Bechtel, B., Xu, Y., Ng, E., 2019. Detecting multi-temporal land cover change and land surface temperature in Pearl River Delta by adopting local climate zone. Urban Clim. 28, 100455.
Wang, Z., Xiao, Z., Tam, C.-Y., Pan, W., Chen, J., Hu, C., Ren, C., Wei, W., Yang, S., 2021. The projected effects of urbanization and climate change on summer thermal environment in Guangdong-Hong Kong-Macao Greater Bay Area of China. Urban Clim. 37 (2021), 100866.
Wen, J., Chen, J., Lin, W., Jiang, B., Xu, S., Lan, J., 2020. Impacts of anthropogenic heat flux and urban land-use change on frontal rainfall near coastal regions: a case study of a rainstorm over the Pearl River Delta, South China. J. Appl. Meteorol. Climatol. 59 (3), 363–379.
Wong, M., Mok, H., Lee, T., 2011. Observed changes in extreme weather indices in Hong Kong. Int. J. Climatol. 31, 2300–2311.
Wu, M., Luo, Y., Chen, F., Wong, W.K., 2019. Observed link of extreme hourly precipitation changes to urbanization over coastal South China. J. Appl. Meteorol. Climatol. 58, 1799–1819.
Xiao, Z., Wang, Z., Huang, M., Luo, X., Liang, Y., Lin, Z., 2020. Urbanization in an underdeveloped city-Nanning, China and its impact on a heavy rainfall event in July. Earth and space. Science 7, e2019EA000991.
Yan, M., Chan, J., Zhao, K., 2020. Impacts of urbanization on the precipitation characteristics in Guangdong Province, China. Adv. Atmos. Sci. 37 (7), 696–706.
Yotagai, A., Kamiguchi, K., Arakawa, O., Hamada, A., Yasutomi, N., Kitoh, A., 2012. APHRODITE: Constructing a Long-Term Daily Gridded Precipitation Dataset for Asia Based on a Dense Network of Rain Gauges. Bulletin of American Meteorological Society.
Zhang, C., Chen, F., Miao, S., Li, Q., Xia, X., Xuan, C., 2009a. Impacts of urban expansion and future green planting on summer precipitation in the Beijing metropolitan area. J. Geophys. Res.-Atmos. 114 (D2).
Zhang, Q., Xu, C., Becker, S., Zhang, Z., Chen, Y., Coulibaly, M., 2009b. Trends and abrupt changes of precipitation maxima in the Pearl River basin, China. Atmos. Sci. Lett. 10, 132–144.
Zhang, Y., Miao, S., Dai, Y., Bornstein, R., 2017. Numerical simulation of urban land surface effects on summer convective rainfall under different UHI intensity in Beijing. J. Geophys. Res.-Atmos. 122 (15), 7851–7868.